Received 5 June 2023; revised 26 November 2023; accepted 8 December 2023. date of current version 22 December 2023.

Digital Object Identifier 10.1109/OJUFFC.2023.3342751

Deep and Complex Vascular Anatomy in the Rat Brain Described With Ultrasound Localization Microscopy in 3D

ARTHUR CHAVIGNON[1], BAPTISTE HEILES[1,2] (Member, IEEE), VINCENT HINGOT[1], CYRILLE ORSET[3], DENIS VIVIEN[3,4], AND OLIVIER COUTURE[1] (Member, IEEE)

[1]Laboratoire d'Imagerie Biomedicale, CNRS, INSERM, Sorbonne Université, 75006 Paris, France
[2]Maresca Laboratory, TU Delft, 2628 CJ Delft, The Netherlands
[3]Etablissement Français du Sang, Physiopathology and Imaging of Neurological Disorders (PhIND), Cyceron, Institut Blood and Brain @ Caen-Normandie (BB@C), INSERM U1237, Caen-Normandy University (UNICAEN), 14000 Caen, France
[4]Department of Clinical Research, Caen-Normandie University Hospital (CHU), 14000 Caen, France

Corresponding author: O. COUTURE (olivier.couture@sorbonne-universite.com)

This work was supported by the European Research Council under the European Union Horizon H2020 Program under Grant 772786-ResolveStroke.

This work involved human subjects or animals in its research. Approval of all ethical and experimental procedures and protocols was granted by the Committee "Comité d'éthique Normandie en matière d'expérimentation animale" under Protocol No. APAFIS #22544, and performed in line with the European Union Directive of 2010 (2010/63/EU).

This article has supplementary downloadable material available at https://doi.org/10.1109/OJUFFC.2023.3342751, provided by the authors.

ABSTRACT Ultrasound Localization Microscopy (ULM) enables imaging microvessels in the brain with a resolution of a few tens of micrometers in-vivo. The planar architecture of arterioles and venules was revealed with a 2D ultrasound scanner in the cortex of the rat brain. However, deeper in the brain, where the vascularization becomes tri-dimensional, 2D imaging remains limited by the elevation projection. In this study, volumetric ultrasound imaging was performed in the craniotomized rat brain to yield 3D ULM *in vivo* within 7.5 min of acquisition with a commercial system. For instance, it highlighted the thalamus or the circle of Willis with small vessels down to 21 μm. Microbubbles tracking also gave access to the 3D velocity vector of blood flow allowing to distinguish flow directions. Volumetric ULM resolved deep complex tri-dimensional vascular structures and was compared to 2D ULM. It is a safe, simple and repeatable system to image wide field of view in the brain.

INDEX TERMS Brain vascular imaging, ultrasound imaging, ultrasound localization microscopy, 3D ultrasound imaging.

I. INTRODUCTION

THE imaging of brain vascularization remains a significant challenge in the study, diagnosis, monitoring and treatment of various cerebral diseases. The blood circulatory system consists of a complex and intricate network of arteries, arterioles, venules and veins interconnected by a vast mesh of small capillaries responsible for delivering oxygen and nutrients to brain cells. Understanding or monitoring its regulation and mechanisms could help the medical care of patients with cerebrovascular troubles. For example, in stroke, vascular characterization enables an accurate diagnosis to engage an efficient treatment.

When needed, brain imaging is performed with MRI or CTscan and highlights the main arteries and veins of the brain. However, it fails at identifying precise arterioles and venules, even with contrast agents. In addition, in an emergency context, these devices are often overbooked and costly.

Recent development in ultrasound imaging [1] has widened the capability of echography. By injecting microbubbles into the bloodstream, Ultrasound Localization Microscopy (ULM) can drastically increase the resolution and sensitivity to the vascular system by localizing isolated microbubbles in blood vessels [2], [3], [4]. It has been extensively demonstrated *in vivo* and particularly in the cortex of small animals [4], [5], [6], [7], [8], [9]. In this region, microvessels have mostly the same orientation and can be almost imaged entirely in the field of view of linear probes. However most of these studies are limited to planar imaging,

where vessels are projected on a thin slice of the organ and their representation remain biased particularly for complex tridimensional vascular structures. Planar ULM imaging has also performed well in the kidney which respects this planar organization [10], [11], [12], while it has been more challenging in tumors where the vessels orientation is more chaotic [13], [14].

In addition, 2D imaging requires multiple tedious image repetitions from different views to characterize the vascularization. With a matrix array of transducers, ultrasound imaging becomes volumetric, with a wide field of view and a quasi-isotropic resolution [15], [16], [17]. Volumetric imaging was then combined with ULM [18], [19] to image the organs' vascularization *in vivo* with complex structures with a single image acquisition [20], [21], [22], [23].

Volumetric ULM requires a high-volume rate to follow microbubbles moving in blood vessels. The system often requires up to 1024 transducers and as many sampling channels [19], [21], [22], [24]. Ultrasound systems are combined and synchronized to get enough sampling channels, which requires costly developments. Other systems used multiplexed matrix probes, reducing the number of sampling channels and making the system easier to use and affordable [20], [25], [26], [27].

In this article, our focus is directed towards describing the striatum and thalamus regions and circle of Willis observed through volumetric ULM. These structures have no particular vessel orientation and could better demonstrate the potential of 3D acquisitions. We describe its implementation with a matrix probe and craniotomy. The visualization of out-of-plane vessels is compared to 2D ULM.

II. METHODS

A. ANIMAL PREPARATION

All animals' experimentations were done under guidelines from the European Community Council (2010/63/EU) and approved by the protocol APAFIS #22544 validated by the French ethics committee ''Comité d'éthique Normandie en matière d'expérimentation animale''. Reporting in the article follows the recommendations of the ARRIVE guidelines.

Sprague Dawley male rats were used (N = 3), 6-7 weeks old. Animals were anaesthetized with isoflurane and placed in a stereotaxic frame to restrain head motion (**Figure 1 A**). The head was shaved and slit (**Figure 1 B**). The parietal bone was slightly drilled on a 1 cm^2 area with a microsurgery drill. A tail vein catheter was installed for microbubbles injection.

B. VOLUMETRIC ULTRASOUND IMAGING FOR ULM

Ultrasound imaging was performed with a multiplexed matrix probe of 1024 elements centered at 7.8 MHz (Vermon, Tours, France) (**Figure 1 C**). The 300 μm width square transducers were aligned in a 32 $\times$ 32 grid and connected to a research ultrafast ultrasound scanner Vantage 256 (Verasonics, Kirkland, USA). The 1024 transducers, divided into 4 sub-apertures, were connected to the 256 sampling channels via individual switches (**Figure 1 C**) of a 4-1 multiplexer (**Figure 1 D**).

Volumes were obtained by compounding 5 bidimensional plane waves to reach a sufficient image quality and volume rate. The tilting angles were (Azimuth, Elevation): {(0, 0); (−5, 0); (5, 0); (0, −5); (0, 5)} in degrees. Because of the multiplexing, each plane wave required 10 transmissions/receptions in the medium to insonify and record echoes of the full field of view [20]. With a PRF of 15 kHz, the final compounded volume rate reached 243 Hz. Each transmission was sent with a 14-volt pulse of 4 half cycles, corresponding to a peak positive pressure of 580 kPa in the water approximately.

For volumetric ULM imaging, 150k volumes were recorded and saved on a disk within 7.5 minutes of acquisition. Volumes were grouped in blocs of 200 frames at 243 Hz. During the long acquisition, boluses of 75 μl of Sonovue (Bracco, Italy) were injected every 60 seconds to maintain a constant microbubbles concentration in the blood.

Post-processing was made on MatLab (The Mathworks, USA, 2019b) and required almost 5 hours for each *in vivo* ULM volume.

C. ULM PROCESSING AND RENDERING

The processing was similar to transcranial ULM and was extensively described and illustrated in [20]. Images were reconstructed offline with a custom delay and sum beamforming implemented in CUDA. Volumes were composed of 70 $\times$ 76 $\times$ 118 voxels of dimension 150 μm $\times$ 150 μm $\times$ 99 μm (lateral x elevation x axial). Microbubbles' signals were enhanced with a singular value decomposition filter [28], [29] and detected with a local maxima detection. Then the center of mass was localized with a radial symmetry algorithm [22] with a resolution lower than the wavelength. Microbubbles were tracked into trajectories of 37 ms minimum persistence, smoothed and interpolated. A 3D velocity vector was assigned for each position by deriving the timeline.

Trajectories were accumulated in an isometric volume of 9.8 μm: when a microbubble travels through a voxel, its intensity is increased by one unity. A hemodynamic matrix was constructed by averaging the velocity in each voxel, with a positive value if the axial component was upward and negative downward.

$$MatVel\,(x,y,z) = \frac{1}{N_{mc}} \sum_{i=1}^{N_{mc}} \|\vec{v}_i\,(x,y,z)\| \ast sign\,(\vec{v}_i\,(x,y,z) \cdot \vec{u}_z)$$

3D renderings were made using Amira Software 2019 (ThermoFisher) with the *Volume Rendering* module after a power law compression between 1/2 and 1/3. For precise analysis, Maximum Intensity Projections (MIP) were made on slabs of 1 mm on MatLab.

D. 2D ULM PROCESSING

To mimic a 2D ULM imaging from the volumetric data, a coronal and sagittal slice were extracted from the

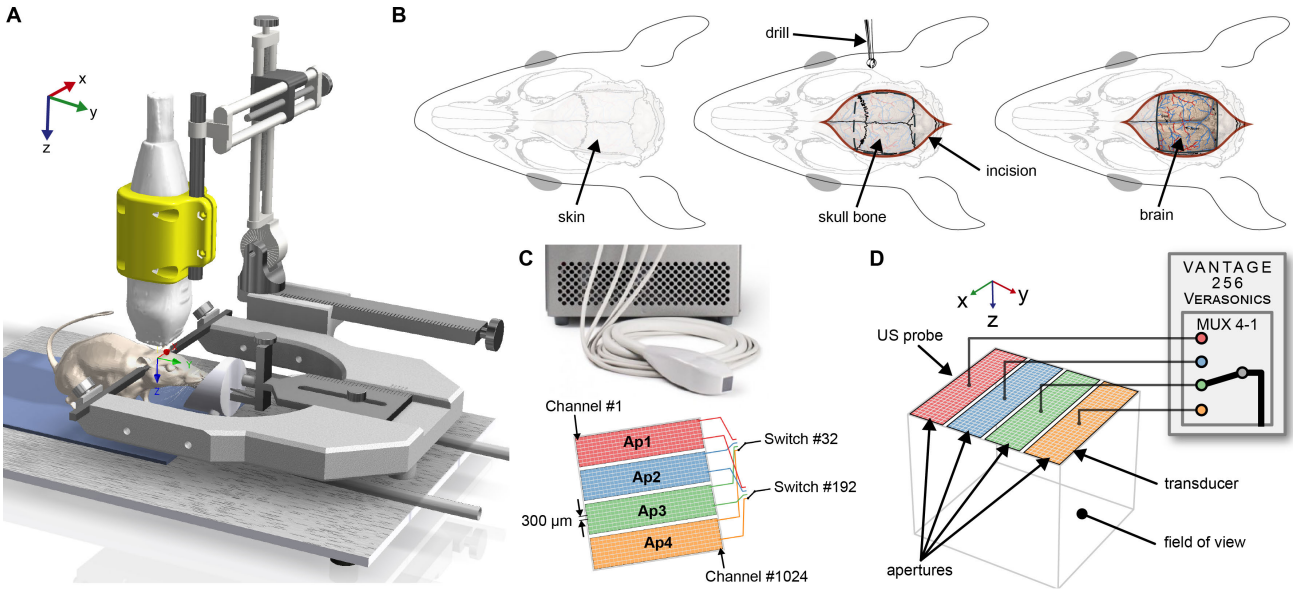

FIGURE 1. **A *In vivo* setup for volumetric ultrafast imaging of the rat brain. B Craniectomy of the rat skull. The skin was open, and the parietal bone drilled along lateral crests and between lambda and bregma. C 7.5 MHz ultrasound matrix probe with 300 μm pitch divided into four sub-apertures. D Connection with the ultrafast ultrasound scanner via a 4-1 multiplexer.**

beamformed volumes. Without focusing lens, the elevation width of this slice can be estimated with the $f_{number} = \frac{Depth}{Aperture}$ used for the reconstruction: 0.2 mm approx. for a $f_{number} = 1$. The 2D images were filtered with singular value decomposition and processed with an open-source 2D ULM processing available at https://github.com/AChavignon/PALA [5]. Microbubbles were detected and localized with a 2D radial symmetry algorithm. Processing parameters were chosen as similarly to the 3D processing.

III. RESULTS

After 7.5 minutes of acquisition, 77 M microbubbles were detected (514 per frame on average) and tracked into 1.1 M trajectories. Once accumulated in super-resolved voxels of 9.8 μm, the vascularization appeared well defined in an 11.2 mm $\times$ 9.9 mm $\times$ 10.8 mm field of view of the brain overlapped with a rat brain surface [30] (**Figure 2 A**). ULM provided clear imaging of vessels deep in the brain by overpassing the tradeoff between penetration and resolution. The parietal bone craniotomy provided a good ultrasound propagation without any shadowed regions, particularly under the sagittal suture covering the superior sagittal sinus and inferior sagittal sinus (**Figure 2 A**). An important lack of perfusion occurred in the cortex due to a vasoconstriction induced by a subarachnoid hemorrhage which occurred during the surgical procedure.

Anatomical regions could be identified by their location in the brain and particular shape. In the anterior ventral part, the thalamus presents a typical radial distribution of vessels (**Figure 2 B, supplementary video 1**). The hippocampus can be identified in the middle of the brain with a C-shape organization (**Figure 2 C**). Deeper and in the axial plane, a major part of the circle of Willis could be imaged (**Figure 2 D**). The striatum shows a more vertical organization in the anterior part of the volume (**Figure 2 E**).

Flow-oriented renderings were used to identify upward and downward flows, typical for venules and arterioles in the cortex and striatum (**Figure 3 A-B**). The velocity rendering was saturated at 30 mm/s with either a positive or negative axial component. Slabs of 1 mm were registered in the stereotaxic coordinates and used to label specific major arteries, such as anterior, middle, and posterior cerebral arteries (Acer, Mcer, and Pcer) in the different coronal sections (**Figure 3 A**). Arteries were identified with vascular atlases of the rat brain [31], and the well-defined mouse atlas from [32] for the labelling (**Figure 3 C**). Smaller cerebral arteries could be labelled for their position, such as the thalamus posterior artery (Thp) and anterior and posterior striate arteries (Astr, Pstr) (**Figure 3 A, C**). The center sagittal slab revealed the superior and inferior sagittal sinus (Sss and Iss), which could not be imaged in [20] due to the sagittal suture of the skull bone.

For clear identification of blood vessels, at least multiple microbubbles must travel through the vessel's lumen. Indeed, due to localization and tracking errors, individual microbubble trajectories cannot be trusted as individual small vessels. However, when multiple microbubbles cross the same voxels, they can be assigned to a blood vessel. The accumulation of similar trajectories reinforces the presence of a blood vessel and enables diameter measurements. Due to requirements in spatial sampling [6], wider vessels require more microbubbles observation for diameter estimation. The Intensity profiles for the sagittal section (**Figure 3 B**) were plotted, representing the maximal number of microbubbles crossing a slab of 0.7 mm (**Figure 3 D**). The two white dotted lines crossed multiple vessels that can be recognized

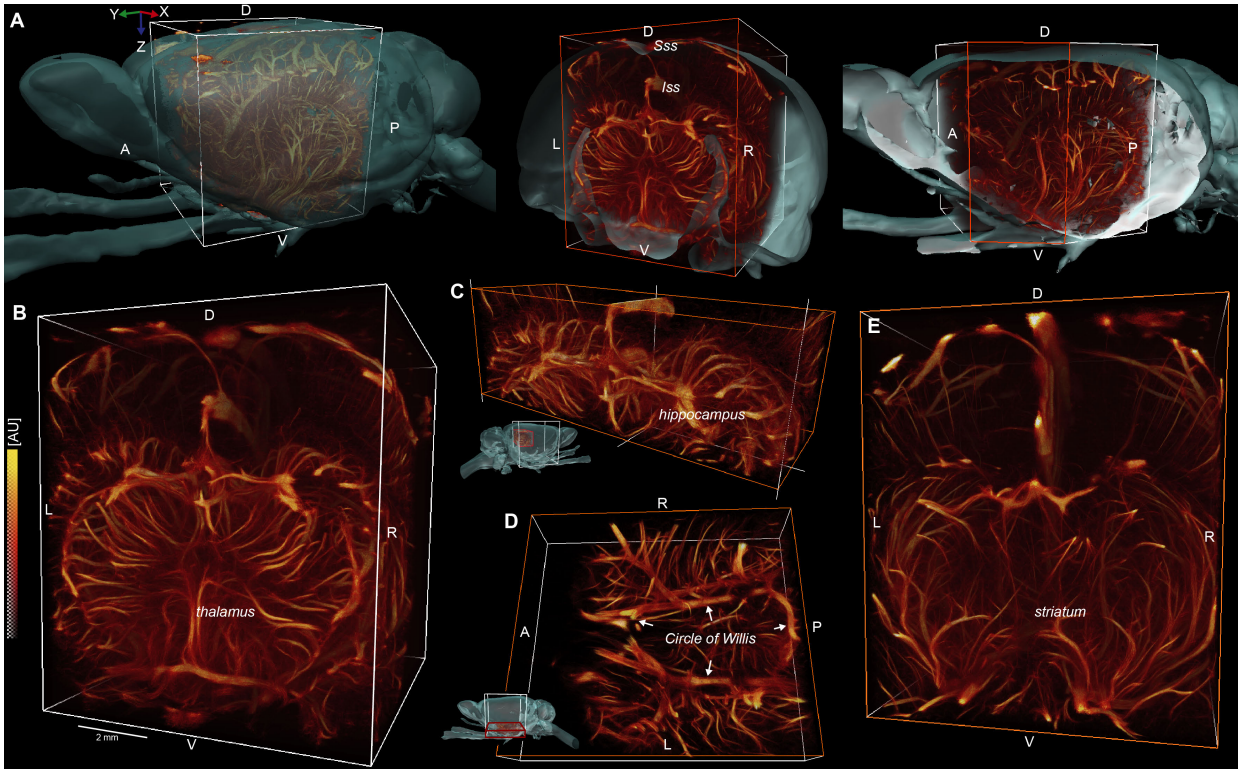

FIGURE 2. A 3D renderings of the rat brain vascularization with the a MRI surface. (Inferiror and superior sagittal sinus: ISS, SSS). B View on the thalamus. C Subregion extracted of the hippocampus. D Zoom in on the circle of Willis in the lower part of the volume. E View on the striatum.

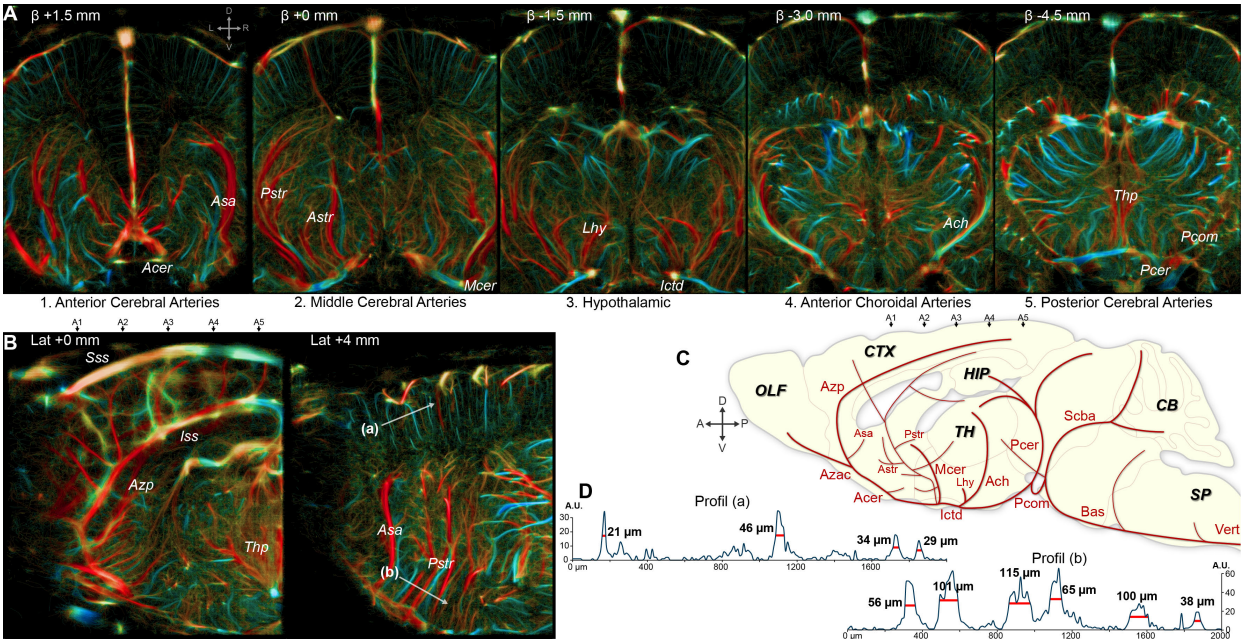

FIGURE 3. A Coronal slabs of 1 mm width of 3D ULM of a craniotomized rat brain. Upward flows were encoded in red, and downward in blue for vessels' identifications with a maximal velocity of 30 mm/s. B Saggital slab of 1 mm width. C Partial atlas of main cerebral arteries of the brain (inspired by Xiong et al., 2017). D Intensity profiles of veins and arteries from the sagittal section, crossing the white dotted arrows (a) and (b) (lat+4mm).

on profiles either in the cortex close to the surface or deeper in the striatum close to the basal forebrain. The full widths at half-maximal were measured for multiple vessels up to 115 μm, with the smallest value of 21 μm (**Figure 3 D**).

The Fourier Shell Correlation (FSC) method was used to estimate the resolution by leveraging the spectral correlation between two subsets of microbubble trajectories [33]. The 2-sigma threshold gave a resolution of 28 μm (**Figure 4**).

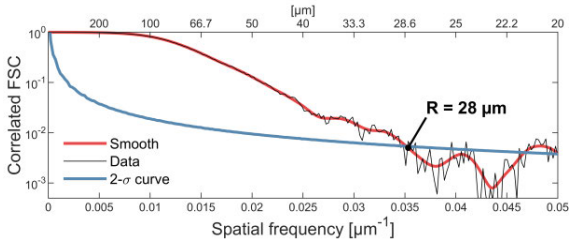

FIGURE 4. Fourier Shell Correlation computed from two subsets of the list of microbubble trajectories. The 2-σ curve gives the maximal consistent spatial frequency.

This minimal vessel diameter detection can be compared to the classical resolution of ultrasound imaging. At 7.8 MHz, the resolution is approximately the wavelength (197 μm). Still, with volumetric ULM, the minimal detectable vessel size is reduced by a factor 9: from 197 to 21 μm approximately, and keeping the same imaging depth which is important for whole brain vascularization imaging.

Finally, a 2D coronal slice was extracted from the beamformed volumes over time and was filtered and reconstructed with a 2D algorithm. **Figure 5 A-B** compares the coronal slice resulting from a maximum intensity projection extracted from the 3D ULM and the results of the 2D ULM processing on the slice extracted from beamformed volume. The same process was done on a sagittal slice (**Figure 5 C-D**). Most in-plane vessels appear in both images with the same intensity and colors. Few bright and out-of-plane vessels are projected on 2D imaging (**Figure 5 B** arrow 1) by the elevation projection. Other vascular structures crossing the imaging plane are missing or biased in the 2D ULM, for example, in the hippocampus (**Figure 5 A** arrow 2) or in the circle of Willis (**Figure 5 B** arrow 3). When blood vessels are orthogonal to the imaging plane, it appears as a bright and sharp spot on the MIP of 3D ULM (**Figure 5 C** arrows 4-5), but these microbubbles become static in 2D imaging and are rejected by the spatio-temporal filtering. Finally, the localization algorithm seems better and more accurate for a few structures which are reconstructed shaper in 2D ULM than in 3D ULM with MIP (**Figure 5 D** arrows 6).

The 3D datasets of microbubble tracks are provided in supplementary materials, along with the codes to visualize them.

IV. DISCUSSION

As demonstrated in recent publications, ULM provides a precise characterization of vascularization *in vivo* with a minimal invasion with a large and deep field-of-view [20], [22], [24], [34] with almost 15 mm depth with 8 MHz matrix array. In this article, we applied 3D ULM in a craniotomized rat to reveal the deep vascularization highly tri-dimensional in the brain (**Figure 2**).

As related in 2D imaging [4], [5], the elevation projection hides flows crossing the plane, which can be inefficient when vascularization is highly tridimensional (**Figure 5**). Temporal filtering failed at detecting these microbubbles, and the tracking cannot be performed. Using a matrix array brings volumetric imaging with high frame rate necessary for microbubbles filtering and tracking which could not be possible with non-real-time 3D such as linear array mechanically translated. By adding a third dimension, it now provides quasi-isotropic sensitivity for vascular imaging, surpassing the limitations of 2D imaging, especially in cases where elevation projection constrains visibility: for example, with complex tri-dimensional vessels in the deep vascular structures of the brain (**Figure 5 B** arrow 3). Slab rendering of 3D ULM reveals a denser vascularization with microbubbles crossing the imaging plane. In addition, 3D imaging provides a full view of the brain within a few minutes of acquisition. Slab renderings using MIP can be realized afterwards and adjusted to the requirements of the analysis. The same experiment with a 2D scanner requires selecting wise imaging planes during the acquisition, and the late analysis would be restricted to the views selected. Moreover, the slab thickness with conventional linear probe is not uniform over the entire depth. Finally, 3D imaging allows post-processing procedures and extensive analyses with no constraints on the acquisition examination.

Working on the brain brings an additional ultrasound problem: imaging under the skull. Indeed, the propagation of ultrasonic waves is altered and attenuated by bone structures and hinders the potential of ULM. In this work, parietal bones were removed to benefit from an acoustic window and highlight the potential of 3D ULM (**Figure 1**). Compared to [20], blood vessels appear here well defined everywhere under the probe without shadowed regions under suture and crests. In particular, the middle cerebral arteries could be imaged with their blood velocity, which is not possible in [20] and [24] because of their location under the bregma suture (**Figure 3**).

The introduction of 3D ULM brought a novel level of resolution for *in vivo* imaging. While most optical imaging technics mainly offered high resolution limited to the surface layer of the brain [35], 3D ULM achieved deeper penetration in the brain by detecting individual vessels with a diameter of a least 21 μm. However, this value is obtained by manually selecting a confident vessel in the volume and cannot be considered as the overall resolution, which would rather measure the separability of vessels. The resolution limit determined by the FSC raised 28 μm, which is seven times smaller than wavelength of 197 μm, which is the limiting factor in resolution in conventional ultrasound imaging. *Ex vivo* techniques can reach a finer resolution [36], [37], [38], [39] but with limited applications to preclinical investigations as they require animal sacrifice.

Volumetric ultrafast imaging is often associated with heavy systems and highly sophisticated and complex data management [15], [17] as they require thousands of sampling channels. The number of sampling channels was reduced to 256 with a multiplexed probe, suitable with a single common ultrasound research scanner reducing the complexity and costs [20], [26], [27]. The maximal volume rate was lower than fully addressed systems [21], [22], [24] but was

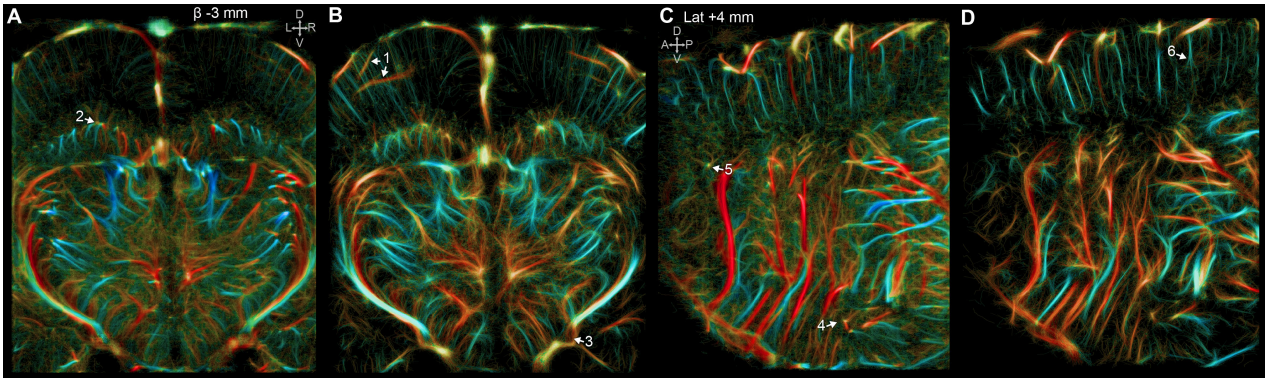

FIGURE 5. Comparison of hemodynamic rendering of slabs of ULM. (A, C) Maximum intensity projections of 3D ULM on a 0.2 mm wide slab. (B, D) 2D ULM obtained after processing 2D slices extracted from the volumetric beamformed data.

high enough to characterize the microvascularization. In our configuration, the maximal velocity resolution was estimated to 73 mm/s, which covers most arterioles and venules' blood velocities [9].

In **Figure 2**, the cortex appeared hypoperfused with a lack of vascularization compared to related publications [4], [8], [9], [22]. During the surgical procedure, a subarachnoid hemorrhage occurred and triggered vasoconstriction inside a major middle part of the cortex. Indeed, skull removal is an invasive and difficult procedure which can damaged the microvascularization of the cortex. This particular example could prove the sensitivity of ULM to microvascularization: when the vascularization is deficient, ULM can reveal it, for example during a vasoconstriction or in ischemic strokes [34], [40].

For small animal imaging, the 8 MHz probe enabled imaging all the brain of the rat, even under the skull [20]. However, for the translation to human, this frequency requires to be reduced to fit the size of the brain and reduce the attenuation of the skull. A phased array matrix could be used to increase the field-of-view keeping small probes. Moreover, aberration correction could facilitate the detection of contrast agents [41]. Finally, imaging framerates should be adjusted to match the blood flow in the brain.

In conclusion, 3D ULM is an emerging technology with a wide range of applications for microvascular imaging [8], [9], [11], [34]. Its precise quantification of microbubble flow in any direction could become a powerful visualization tool for organs and pathologies lacking the planar vascular organization, such as tumors, liver, pancreas and deep cerebral regions.

The imaging quality obtained in the craniotomized rat brain demonstrated the potential of this technic for deep 3D vascularization imaging. Many developments are still required to obtain the same quality on *in vivo* microvascular disease with minimal invasiveness, with motion, skull aberration, and accurate diagnosis.

V. SUPPLEMETARY MATERIALS

The 1.1 M microbubbles' tracks in 3D available with the publication at https://zenodo.org/records/10204813. A processing script (MatLab) is provided to reconstruct the intensity rendering matrix with an adjustable voxel size.

VI. ACKNOWLEDGMENT

This study was performed with the technical and scientific support of the PhIND, ESRP, the Institute BB@C.

VII. AUTHORS CONTRIBUTIONS

All authors designed the research. AC developed the acquisition sequence. BH developed the surgical procedure and the ULM reconstruction. AC, VH and CO did the experiments. AC processed and analyzed the data. All the authors discussed the results and wrote the paper.

VIII. COMPETING INTERESTS

AC, CO, DV, BH declared having no competing interest. OC is depositor of the ultrasound super-resolution patent / FR2011/052810. VH and OC are involved in the startup ResolveStroke, which holds several patents.

IX. ACRONYMS

CB	cerebellum
CTX	cortex
HIP	hippocampus
OLF	olfactory bulb
TH	thalamus
Acer	anterior cerebral artery
Ach	anterior choroidal artery
Asa	ascending septal artery
Astr	anterior striate artery
Azac	azygos of anterior cerebral artery
Azp	azygos pericallosal artery
Bas	basilar artery
Ictd	internal carotid artery
Iss	internal sagittal sinus
Lhy	lateral hypothalamic artery
Mcer	middle cerebral artery
Pcer	posterior cerebral artery
Pcom	posterior communicating artery
Pstr	posterior striate artery
Scba	superior cerebellar artery
Sss	superior sagittal sinus
Thp	thalamoperforating artery
Vert	vertebral artery

REFERENCES

[1] M. Tanter and M. Fink, "Ultrafast imaging in biomedical ultrasound," *IEEE Trans. Ultrason., Ferroelectr., Freq. Control*, vol. 61, no. 1, pp. 102–119, Jan. 2014, doi: 10.1109/TUFFC.2014.2882.

[2] K. Christensen-Jeffries et al., "Super-resolution ultrasound imaging," *Ultrasound Med. Biol.*, vol. 46, no. 4, pp. 865–891, Apr. 2020, doi: 10.1016/j.ultrasmedbio.2019.11.013.

[3] O. Couture, V. Hingot, B. Heiles, P. Muleki-Seya, and M. Tanter, "Ultrasound localization microscopy and super-resolution: A state of the art," *IEEE Trans. Ultrason., Ferroelectr., Freq. Control*, vol. 65, no. 8, pp. 1304–1320, Aug. 2018, doi: 10.1109/TUFFC.2018.2850811.

[4] C. Errico et al., "Ultrafast ultrasound localization microscopy for deep super-resolution vascular imaging," *Nature*, vol. 527, no. 7579, pp. 499–502, Nov. 2015, doi: 10.1038/nature16066.

[5] B. Heiles, A. Chavignon, V. Hingot, P. Lopez, E. Teston, and O. Couture, "Performance benchmarking of microbubble-localization algorithms for ultrasound localization microscopy," *Nature Biomed. Eng.*, vol. 6, no. 5, pp. 605–616, Feb. 2022, doi: 10.1038/s41551-021-00824-8.

[6] V. Hingot, C. Errico, B. Heiles, L. Rahal, M. Tanter, and O. Couture, "Microvascular flow dictates the compromise between spatial resolution and acquisition time in ultrasound localization microscopy," *Sci. Rep.*, vol. 9, no. 1, p. 1, Feb. 2019, doi: 10.1038/s41598-018-38349-x.

[7] L. Milecki et al., "A deep learning framework for spatiotemporal ultrasound localization microscopy," *IEEE Trans. Med. Imag.*, vol. 40, no. 5, pp. 1428–1437, May 2021, doi: 10.1109/TMI.2021.3056951.

[8] N. Renaudin, C. Demené, A. Dizeux, N. Ialy-Radio, S. Pezet, and M. Tanter, "Functional ultrasound localization microscopy reveals brain-wide neurovascular activity on a microscopic scale," *Nature Methods*, vol. 19, no. 8, pp. 1004–1012, Aug. 2022, doi: 10.1038/s41592-022-01549-5.

[9] C. Bourquin, J. Porée, F. Lesage, and J. Provost, "In vivo pulsatility measurement of cerebral microcirculation in rodents using dynamic ultrasound localization microscopy," *IEEE Trans. Med. Imag.*, vol. 41, no. 4, pp. 782–792, Apr. 2022, doi: 10.1109/TMI.2021.3123912.

[10] S. Bodard et al., "Ultrasound localization microscopy of the human kidney allograft on a clinical ultrasound scanner," *Kidney Int.*, vol. 103, no. 5, pp. 930–935, May 2023, doi: 10.1016/j.kint.2023.01.027.

[11] L. Denis et al., "Sensing ultrasound localization microscopy for the visualization of glomeruli in living rats and humans," *eBioMedicine*, vol. 91, May 2023, Art. no. 104578, doi: 10.1016/j.ebiom.2023.104578.

[12] I. Taghavi et al., "Ultrasound super-resolution imaging with a hierarchical Kalman tracker," *Ultrasonics*, vol. 122, May 2022, Art. no. 106695, doi: 10.1016/j.ultras.2022.106695.

[13] F. Lin, S. E. Shelton, D. Espíndola, J. D. Rojas, G. Pinton, and P. A. Dayton, "3-D ultrasound localization microscopy for identifying microvascular morphology features of tumor angiogenesis at a resolution beyond the diffraction limit of conventional ultrasound," *Theranostics*, vol. 7, no. 1, pp. 196–204, 2017, doi: 10.7150/thno.16899.

[14] T. Opacic et al., "Motion model ultrasound localization microscopy for preclinical and clinical multiparametric tumor characterization," *Nature Commun.*, vol. 9, no. 1, p. 1, Apr. 2018, doi: 10.1038/s41467-018-03973-8.

[15] J. A. Jensen et al., "SARUS: A synthetic aperture real-time ultrasound system," *IEEE Trans. Ultrason., Ferroelectr., Freq. Control*, vol. 60, no. 9, pp. 1838–1852, Sep. 2013, doi: 10.1109/TUFFC.2013.2770.

[16] L. Petrusca et al., "Fast volumetric ultrasound B-mode and Doppler imaging with a new high-channels density platform for advanced 4D cardiac imaging/therapy," *Appl. Sci.*, vol. 8, no. 2, p. 200, Jan. 2018, doi: 10.3390/app8020200.

[17] J. Provost et al., "3D ultrafast ultrasound imaging in vivo," *Phys. Med. Biol.*, vol. 59, no. 19, Oct. 2014, Art. no. 19, doi: 10.1088/0031-9155/59/19/L1.

[18] S. Harput et al., "3-D super-resolution ultrasound imaging with a 2-D sparse array," *IEEE Trans. Ultrason., Ferroelectr., Freq. Control*, vol. 67, no. 2, pp. 269–277, Feb. 2020, doi: 10.1109/TUFFC.2019.2943646.

[19] B. Heiles et al., "Ultrafast 3D ultrasound localization microscopy using a 32 × 32 matrix array," *IEEE Trans. Med. Imag.*, vol. 38, no. 9, pp. 2005–2015, Sep. 2019, doi: 10.1109/TMI.2018.2890358.

[20] A. Chavignon, B. Heiles, V. Hingot, C. Orset, D. Vivien, and O. Couture, "3D transcranial ultrasound localization microscopy in the rat brain with a multiplexed matrix probe," *IEEE Trans. Biomed. Eng.*, vol. 69, no. 7, pp. 2132–2142, Jul. 2022, doi: 10.1109/TBME.2021.3137265.

[21] O. Demeulenaere et al., "Coronary flow assessment using 3-dimensional ultrafast ultrasound localization microscopy," *JACC, Cardiovascular Imag.*, vol. 15, no. 7, pp. 1193–1208, Jul. 2022, doi: 10.1016/j.jcmg.2022.02.008.

[22] B. Heiles et al., "Volumetric ultrasound localization microscopy of the whole rat brain microvasculature," *IEEE Open J. Ultrason., Ferroelectr., Freq. Control*, vol. 2, pp. 261–282, 2022, doi: 10.1109/OJUFFC.2022.3214185.

[23] U.-W. Lok et al., "Three-dimensional ultrasound localization microscopy with bipartite graph-based microbubble pairing and Kalman-filtering-based tracking on a 256-channel verasonics ultrasound system with a 32 × 32 matrix array," *J. Med. Biol. Eng.*, vol. 42, no. 6, pp. 767–779, Oct. 2022, doi: 10.1007/s40846-022-00755-y.

[24] J. R. McCall, F. Santibanez, H. Belgharbi, G. F. Pinton, and P. A. Dayton, "Non-invasive transcranial volumetric ultrasound localization microscopy of the rat brain with continuous, high volume-rate acquisition," *Theranostics*, vol. 13, no. 4, pp. 1235–1246, 2023, doi: 10.7150/thno.79189.

[25] M. Bernal, B. Cunitz, D. Rohrbach, and R. Daigle, "High-frame-rate volume imaging using sparse-random-aperture compounding," *Phys. Med. Biol.*, vol. 65, no. 17, Sep. 2020, Art. no. 175002, doi: 10.1088/1361-6560/ab9372.

[26] C. Brunner et al., "A platform for brain-wide volumetric functional ultrasound imaging and analysis of circuit dynamics in awake mice," *Neuron*, vol. 108, no. 5, pp. 861.e7–875.e7, Dec. 2020, doi: 10.1016/j.neuron.2020.09.020.

[27] J. Yu, H. Yoon, Y. M. Khalifa, and S. Y. Emelianov, "Design of a volumetric imaging sequence using a vantage-256 ultrasound research platform multiplexed with a 1024-element fully sampled matrix array," *IEEE Trans. Ultrason., Ferroelectr., Freq. Control*, vol. 67, no. 2, pp. 248–257, Feb. 2020, doi: 10.1109/TUFFC.2019.2942557.

[28] C. Demené et al., "Spatiotemporal clutter filtering of ultrafast ultrasound data highly increases Doppler and fUltrasound sensitivity," *IEEE Trans. Med. Imag.*, vol. 34, no. 11, pp. 2271–2285, Nov. 2015, doi: 10.1109/TMI.2015.2428634.

[29] Y. Desailly, A.-M. Tissier, J.-M. Correas, F. Wintzenrieth, M. Tanter, and O. Couture, "Contrast enhanced ultrasound by real-time spatiotemporal filtering of ultrafast images," *Phys. Med. Biol.*, vol. 62, no. 1, pp. 31–42, Jan. 2017, doi: 10.1088/1361-6560/62/1/31.

[30] E. A. Papp, T. B. Leergaard, E. Calabrese, G. A. Johnson, and J. G. Bjaalie, "Waxholm space atlas of the sprague dawley rat brain," *NeuroImage*, vol. 97, pp. 374–386, Aug. 2014, doi: 10.1016/j.neuroimage.2014.04.001.

[31] O. U. Scremin, "Cerebral vascular system," in *The Rat Nervous System*. Amsterdam, The Netherlands: Elsevier, 2004, pp. 1167–1202, doi: 10.1016/B978-012547638-6/50034-1.

[32] B. Xiong et al., "Precise cerebral vascular atlas in stereotaxic coordinates of whole mouse brain," *Frontiers Neuroanatomy*, vol. 11, p. 128, Dec. 2017, doi: 10.3389/fnana.2017.00128.

[33] V. Hingot, A. Chavignon, B. Heiles, and O. Couture, "Measuring image resolution in ultrasound localization microscopy," *IEEE Trans. Med. Imag.*, vol. 40, no. 12, pp. 3812–3819, Dec. 2021, doi: 10.1109/TMI.2021.3097150.

[34] A. Chavignon, V. Hingot, C. Orset, D. Vivien, and O. Couture, "3D transcranial ultrasound localization microscopy for discrimination between ischemic and hemorrhagic stroke in early phase," *Sci. Rep.*, vol. 12, no. 1, p. 14607, Aug. 2022, doi: 10.1038/s41598-022-18025-x.

[35] A. Y. Shih, J. D. Driscoll, P. J. Drew, N. Nishimura, C. B. Schaffer, and D. Kleinfeld, "Two-photon microscopy as a tool to study blood flow and neurovascular coupling in the rodent brain," *J. Cerebral Blood Flow Metabolism*, vol. 32, no. 7, pp. 1277–1309, Jul. 2012, doi: 10.1038/jcbfm.2011.196.

[36] A. Ertürk et al., "Three-dimensional imaging of solvent-cleared organs using 3DISCO," *Nature Protocols*, vol. 7, no. 11, pp. 1983–1995, Nov. 2012, doi: 10.1038/nprot.2012.119.

[37] R. Hlushchuk et al., "Innovative high-resolution microCT imaging of animal brain vasculature," *Brain Struct. Function*, vol. 225, no. 9, pp. 2885–2895, Dec. 2020, doi: 10.1007/s00429-020-02158-8.

[38] S. M. Jorgensen, O. Demirkaya, and E. L. Ritman, "Three-dimensional imaging of vasculature and parenchyma in intact rodent organs with X-ray micro-CT," *Amer. J. Physiol.-Heart Circulatory Physiol.*, vol. 275, no. 3, pp. H1103–H1114, Sep. 1998, doi: 10.1152/ajpheart.1998.275.3.H1103.

[39] N. Renier, Z. Wu, D. J. Simon, J. Yang, P. Ariel, and M. Tessier-Lavigne, "IDISCO: A simple, rapid method to immunolabel large tissue samples for volume imaging," *Cell*, vol. 159, no. 4, pp. 896–910, Nov. 2014, doi: 10.1016/j.cell.2014.10.010.

[40] V. Hingot et al., "Early ultrafast ultrasound imaging of cerebral perfusion correlates with ischemic stroke outcomes and responses to treatment in mice," *Theranostics*, vol. 10, no. 17, pp. 7480–7491, 2020, doi: 10.7150/thno.44233.

[41] C. Demené et al., "Transcranial ultrafast ultrasound localization microscopy of brain vasculature in patients," *Nature Biomed. Eng.*, vol. 5, no. 3, pp. 219–228, Mar. 2021, doi: 10.1038/s41551-021-00697-x.